Gate-Controlled Large Resistance Switching Driven by Charge-Density Wave in 1*T*-TaS_2/2*H*-MoS_2 Heterojunctions

Mehak Mahajan, Krishna Murali, Nikhil Kawatra, and Kausik Majumdar*
Department of Electrical Communication Engineering, Indian Institute of Science, Bangalore 560012, India

(Received 30 October 2018; revised manuscript received 10 December 2018; published 12 February 2019)

1*T*-TaS_2 is a layered material that exhibits charge density wave (CDW) -induced distinct electrical resistivity phases and has attracted a lot of attention for interesting device applications. However, such resistivity switching effects are often weak, and cannot be modulated by an external gate voltage — limiting their widespread usage. Using a back-gated 1*T*-TaS_2/2*H*-MoS_2 heterojunction, we show that the usual resistivity switching in TaS_2 due to different phase transitions is accompanied with a surprisingly strong modulation in the Schottky barrier height (SBH) at the TaS_2/MoS_2 interface — providing an additional knob to control the degree of the phase-transition-driven resistivity switching by an external gate voltage. In particular, the commensurate (*C*) to triclinic (*T*) phase transition results in an increase in the SBH owing to a collapse of the Mott gap in TaS_2. The change in SBH allows us to estimate an electrical Mott-gap opening of approximately 71 ± 7 meV in the *C* phase of TaS_2. On the other hand, the nearly commensurate (*NC*) to incommensurate (*IC*) phase transition results in a suppression in the SBH, and the heterojunction shows a gate-controlled resistivity switching ratio up to 17.3, which is approximately 14.5 times higher than that of stand-alone TaS_2. The findings mark an important step forward showing a promising pathway to externally control as well as amplify the CDW-induced resistivity switching. This will boost device applications that exploit these phase transitions, such as ultra-broadband photodetection, negative differential conductance, fast oscillator and threshold switching in neuromorphic circuits.

DOI: 10.1103/PhysRevApplied.11.024031

I. INTRODUCTION

Transition-metal dichalcogenides are emerging as pertinent materials for applications in high-performance flexible electronics and optoelectronics [1–3]. 1*T*-TaS_2 is a distinct layered material that exhibits multiple conductivity phases resulting from strong electron-phonon and electron-electron interactions. This material hosts a wide variety of charge density wave (CDW) [4,5] states and the CDW amplitude is significant in the 1*T*-polytype as compared to the 2*H*-polytype of TaS_2 [6,7]. Depending on the temperature of the 1*T*-TaS_2 crystal, CDW exists in different phases subject to alignment with the underlying lattice [6,8–10]. As the temperature is reduced below 550 K, the metallic crystal undergoes a CDW phase transition, however, the CDW remains incommensurate (*IC*) with the underlying crystal lattice. On further cooling, it undergoes an IC to nearly-commensurate (*NC*) CDW phase transition at 340 K, and an *NC* to commensurate (*C*) phase transition at 180 K. The *NC* to *C* transition is accompanied with a Mott transition resulting in strong suppression of conductivity. On heating, the crystal undergoes a new phase transition, from the *C* phase to the triclinic (*T*) phase appearing at 223 K [11–13], followed by *T* to *NC*, and *NC* to *IC* phase transitions at 283 and 353 K, respectively. The different CDW phase transitions can also be controlled by pressure [8,14], doping [15,16], thickness [17,18], and photoexcitation [9,19].

Among these different phase transitions, the *C*-*T* transition is of great scientific interest due to a large resistivity switching of more than an order of magnitude [7,8,18] owing to a Mott-gap opening associated with the phase transition. While the Mott-gap opening has been extracted by several reports using various optical techniques [9,10,20–25], a direct estimation of the electrical gap from transport measurement of a TaS_2 device is missing. On the contrary, the *NC*-*IC* transition can be electrically driven while operating at room temperature and thus has attracted a lot of attention in device applications, including wideband photodetectors [26], fast oscillators [27], and neuromorphic circuits [28]. However, there are two intrinsic bottlenecks with such resistivity switching. First, the resistivity switching ratio during the *NC*-*IC* phase transition is quite weak (<2) [7,8,18]. Second, the phase transition-driven resistivity switching of TaS_2 cannot be controlled by an external gate voltage. Hence, improving the switching ratio in the *NC*-*IC* phase transition and adding a possible gate controllability would be of great importance for the advancement of these applications.

*kausikm@iisc.ac.in

In order to address these issues, we employ a $1T$-$TaS_2/2H$-MoS_2 heterojunction (lattice mismatch of approximately 6.33% [29,30]) in a back-gated field effect transistor (FET) structure. We show that the TaS_2/MoS_2 interface exhibits a low-barrier, high-performance van der Waals (vdW) electrical contact [31–36], which is promising for the pathway toward "all-2D" flexible devices. We also demonstrate that both the *C*-*T* and *NC*-*IC* phase transitions not only result in a change in the resistivity in the TaS_2 film, but also bring about a change in the Schottky barrier height (SBH) at the TaS_2/MoS_2 interface. This allows us to control the phase-transition-driven carrier transport through the heterojunction device by the application of a gate voltage. The *C*-*T* phase transition results in an increase in the SBH, which allows us to electrically estimate the Mott-gap opening in $1T$-TaS_2 at the *C* phase. On the other hand, the *NC*-*IC* phase transition reduces the SBH at the TaS_2/MoS_2 interface, which, depending on the gate voltage applied, enhances the switching ratio by a factor as much as 14.5 times compared with $1T$-TaS_2 control.

II. RESULTS AND DISCUSSIONS

2H-MoS_2 is a layered transition-metal dichalcogenide (TMDC) semiconductor, which is appealing as a channel material in electronic device applications owing to its appreciable band gap, moderate carrier mobility, and channel-length scalability. The heterojunction device used in this work is schematically shown in Fig. 1(a), where a back-gated MoS_2 channel is formed with asymmetric contacts, namely, Ni and TaS_2 contacts on two different sides. We note that Ni makes good electrical contact with MoS_2 [37–39] (see S1 within the Supplemental Material [40]) owing to efficient interfacial charge transfer resulting from strong hybridization of partially filled Ni-3*d* and S-3*p* orbitals [39]. By switching the polarity of the drain voltage, we study characteristics of the carrier injection through the TaS_2/MoS_2 contact interface while taking the Ni/MoS_2 junction of the same device as the reference interface. To fabricate the heterojunction device, we first exfoliate few-layer $2H$-MoS_2 flakes on a 285-nm-thick SiO_2-coated heavily-doped Si substrate. We next transfer thin layers of $1T$-TaS_2 on top of the MoS_2 flake under a microscope using a micromanipulator. The contact electrodes are patterned by electron-beam lithography, followed by electron-beam evaporation of Ni(10 nm)/Au(50 nm), and subsequent lift-off. Figure 1(b) shows the optical image of the device after completion of fabrication. The top panel of Fig. 1(c) depicts the corresponding thickness mapping image using AFM. The bottom panel of Fig. 1(c) shows the thickness of the MoS_2 and the TaS_2 flakes are 6.4 and 43.6 nm, respectively, as measured along the green dashed arrow. The devices reported in this work are measured multiple times over a period of several weeks and no noticeable degradation of the device characteristics is observed due to surface oxidation and other ambience-induced effects.

Raman spectroscopy is a useful tool to characterize CDW phase transitions in $1T$-TaS_2 [41–45]. When the crystal has not undergone any CDW phase transition, due to the high symmetry of the crystal, specific zone center phonons participate in the first-order Raman scattering in order to maintain both energy and momentum conservation. However, once a CDW phase change sets in, the lattice distorts, reducing the translational symmetry of the crystal. This relaxes the condition of first-order Raman scattering at the zone center and results in a large number of Raman active vibrational modes [41]. Figure 2(a) shows

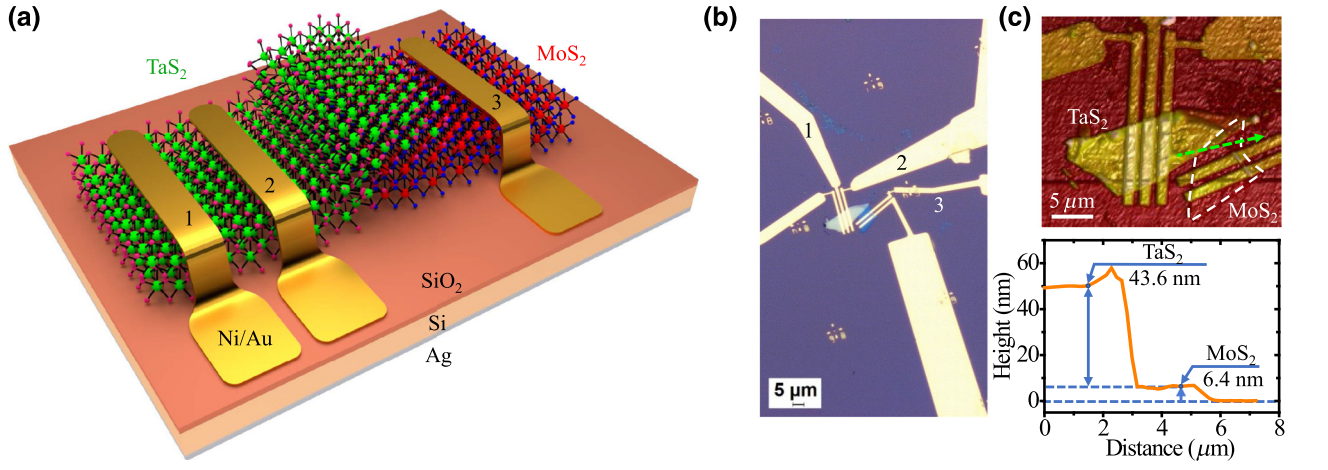

FIG. 1. $1T$-$TaS_2/2H$-MoS_2 heterojunction. (a) Schematic of the device with terminals 1 and 2 probing the TaS_2 control device (TS12) and terminals 2 and 3 probing the heterojunction device (H23). (b) Optical image of the fabricated device. Scale bar: 5 μm. (c) Top panel: AFM thickness-mapping image of the heterojunction device. Scale bar: 5 μm. Bottom panel: Thicknesses of the MoS_2 and TaS_2 flakes along the green dashed arrow in the top panel.

the acquired Raman spectra from 1*T*-TaS_2 in the heating cycle using a 532-nm laser excitation at 193 K (*C* phase) and 300 K (*NC* phase), which are in agreement with previous reports [41,42,45]. In the *C* phase, the distinct Raman peaks at the lower frequencies (between 90 and 140 cm^{-1}) result from acoustic branches and directly correlate with the signature of the commensurate nature of the *C* phase. The higher frequency peaks (between 200 to 400 cm^{-1}) originate from optical phonons [42], and can be observed in both *C* and *NC* phases.

Figure 2(b) depicts the resistance (*R*)-temperature (*T*) characteristics of a representative two-probe TaS_2 device (in the inset) in vacuum in the heating cycle under a small electric field condition. Each layer of 1*T*-TaS_2 crystal structure is composed of tantalum (Ta) atoms, which are surrounded by sulfur atoms in an octahedral arrangement [13]. The high resistance state at low temperature results from the *C* phase, where the David-star structure [6,46], as depicted in Fig. 2(c), forms a commensurate structure with the underlying lattice. This commensurate phase results from the inward displacement of the 12 Ta atoms, located at the star corners, toward the 13th Ta atom at the center of the star. The atomic displacement results in the deformation in the structure, including a swelling at the star center [30,47]. The reduction in the interatomic distance strengthens the bonds inside the David-star in comparison to the bonds outside the star, resulting in the disintegration of the band structure into submanifolds. The 12-corner Ta atoms of the star contribute electrons to the two three-band submanifolds in the valence band, whereas the 13th atom at

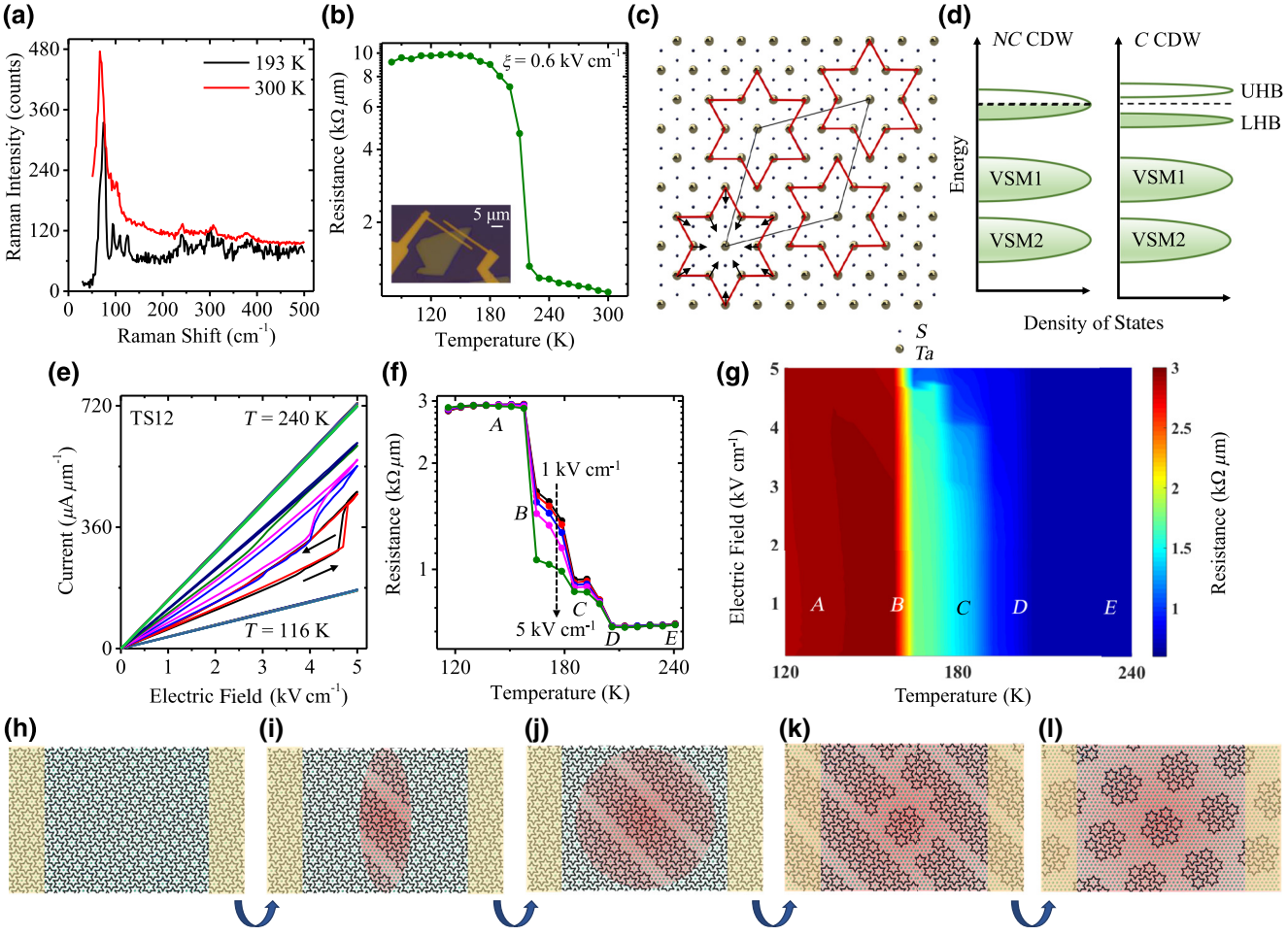

FIG. 2. Electrical tuning of phase transitions in 1*T*-TaS_2. (a) Raman shift of 1*T*-TaS_2 in the *NC* phase (at 300 K in red) and in *C* phase (at 193 K in black) during the heating cycle. (b) Temperature-dependent resistance of a representative TaS_2 flake under low-field condition. Inset: Optical image of the device. (c) David-star structure formation in the *C* phase of 1*T*-TaS_2. (d) Hubbard model of 1*T*-TaS_2 depicting Mott-gap opening. UHB and LHB denote the upper and the lower Hubbard bands, respectively. VSM1 and VSM2 represent the first and second valence band submanifolds, respectively. (e) Current-electric field characteristics of 1*T*-TaS_2 two probe device [TS12—probing terminals 1 and 2 in Figs. 1(a) and 1(b)] in the temperature range 116–240 K. The black arrows indicate the bias sweep direction. (f) Resistance-temperature plot of the forward sweep in (e) indicating multiple resistance states. (g) Color plot of resistance in the temperature-field space. (h)–(l) Joule-heating-induced localized phases of the device giving rise to multiple resistance states in (f).

the center of the star contributes one electron to the submanifold in the conduction band [Fig. 2(d)—left panel]. It has been suggested that the spin-orbit coupling forces further reconstruction in the band structure and result in a unique narrow band at the Fermi level that is partially filled [48,49]. This facilitates electron-electron interaction-induced Mott transition in the lattice and a Mott gap opens up [Fig. 2(d)—right panel] [47,49].

A. Electrically accessing different 1*T*-TaS_2 phases

In order to electrically access the different CDW phases of TaS_2, we next apply a high field across probes 1 and 2 of the TaS_2 device TS12 in Fig. 1(a). The hysteretic bistable switching, as observed in Fig. 2(e), is indicative of an external-bias-controlled phase change of the TaS_2 flake. The sharp change in resistance is observed around 160 K [Fig. 2(f)], which is lower than the *C*-*T* phase transition temperature (approximately 220 K) under low field in Fig. 2(b). This suggests that the Joule heating-induced increase in local temperature plays a key role in the phase change. A color phase plot of the different resistance states in the temperature-electric field space is shown in Fig. 2(g).

We construct a simple model for the multistate resistance switching in the TaS_2 flake, as explained in Figs. 2(h)–2(l). Initially, at low temperature, the whole flake is in *C* phase, with linear current-field characteristics [Fig. 2(h)]. This situation is denoted by point *A* in Figs. 2(f) and 2(g). As the sample is heated close to the *C*-*T* phase transition temperature (T_{CT}), the current-induced Joule heating drives the local temperature at the central part of the flake (which is farthest from the contact heat sinks) at a higher value than the rest of the flake. Note that in the *C* phase, in particular, close to T_{CT}, an increase in the temperature results in a steep reduction in the lattice component of the thermal conductivity, suppressing the overall thermal conductivity [50]. This provides a positive feedback and further helps to increase the local temperature. Eventually, the temperature of the central part is driven beyond T_{CT}, forcing a local *C*-*T* phase transition (point *B*), as schematically depicted in Fig. 2(i). This corresponds to a steep jump in the overall resistance of the sample. With a further increase in the drain field or heating of the sample (point *C*), the local temperature of the surrounding portion also increases, causing a gradual increase in the size of the central *T* phase region [Fig. 2(j)], and, in turn, results in the gradual reduction in the resistance. When the temperature and field are increased further, the whole flake is eventually converted into *T* phase [Fig. 2(k)], and no further change in resistance is observed beyond this point (point *D*). At higher temperature (point *E*—beyond 283 K lattice temperature), the whole flake transforms into *NC* phase [Fig. 2(l)], however, *T*-*NC* phase transition has an almost negligible impact on any further change in resistance [11,13]. The above-mentioned Joule heating-induced phase transition mechanism is qualitatively supported by the hysteresis observed in the current-field plot in Fig. 2(e). The flake undergoes a *C*-*T* phase transition due to Joule heating in the forward sweep. When the field is withdrawn, Joule heating is suppressed, but the flake does not immediately come back to high-resistance *C* phase until the flake cools down below 180 K, resulting in hysteresis.

B. Efficient carrier injection by 1*T*-TaS_2 contact

We next explore the carrier injection efficiency from 1*T*-TaS_2 to 2*H*-MoS_2 in the heterojunction device (H23) shown in Fig. 1(a), by probing terminals 2 and 3. We take TaS_2 and Ni as the source (*S*) and the drain (*D*), respectively, in the rest of the paper. Thus, owing to the asymmetric design of the device, for $V_D(=V_{32}) > 0$, electrons are injected from the TaS_2 contact, while for $V_D < 0$, electrons are injected from Ni into the MoS_2 channel. Hence, by switching the polarity of V_D, we can probe the carrier injection from individual contacts, as schematically

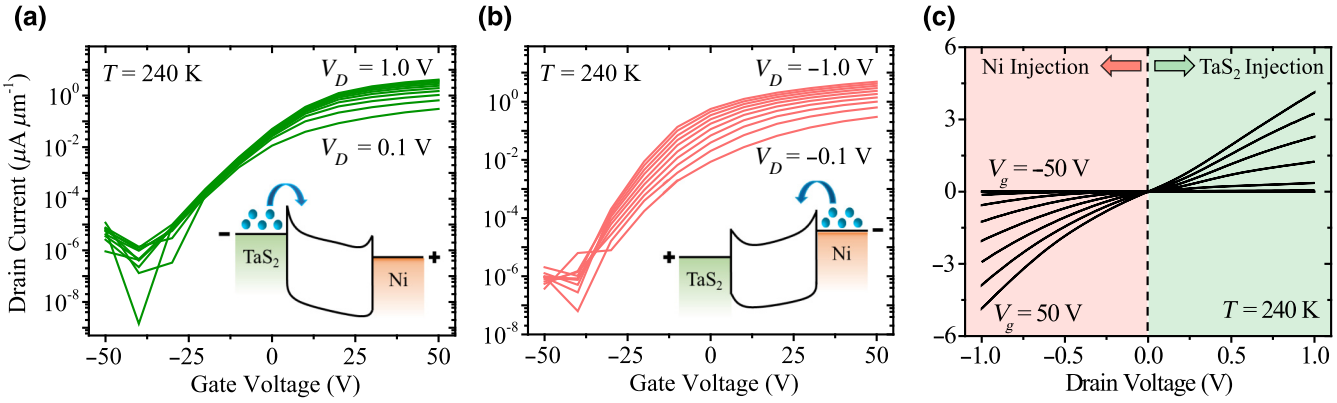

FIG. 3. Current-voltage characteristics of the heterojunction device H23. Probing terminals 2 and 3 in Figs. 1(a) and 1(b). (a),(b) Transfer characteristics at 240 K (*T* phase) at different drain voltages, with (a) $V_D > 0$ (Ni is under positive bias and TaS_2 is sourcing electrons) and (b) $V_D < 0$ (TaS_2 is under positive bias and Ni is sourcing electrons). (c) Output characteristics of the same device.

depicted in the insets of Figs. 3(a) and 3(b). The transfer characteristics of the device for the two cases, shown in Figs. 3(a) and 3(b) at $T = 240\,\mathrm{K}$ (T phase), indicate an on-off ratio in excess of 10^6, regardless of the carriers being injected from Ni or TaS_2. Figure 3(c) shows the output characteristics at different back-gate voltages (V_g). We clearly observe that the magnitude of the drive current is similar for both TaS_2 and Ni injection cases, suggesting excellent carrier injection efficiency of the TaS_2/MoS_2 interface. Such highly efficient carrier injection from the TaS_2/MoS_2 junction is promising for vdW-vdW contact engineering.

C. Modulating drive current by *C-T* phase transition

We next turn our attention to the control of the carrier injection as the phase of the $1T$-TaS_2 source undergoes a C-T phase transition. The two different situations are schematically depicted in Figs. 4(a) and 4(b). Note that in this heterojunction device, the overall current density through the TaS_2 source is smaller compared to the high-field case discussed in Fig. 2(e) (TS12) owing to the series resistance offered by the MoS_2 channel, and hence the role of local Joule heating in the phase transition in the TaS_2 source can be ruled out. This results in a more uniform phase transition in the TaS_2 source controlled by the external temperature. The measured device current with $V_D > 0$ and $V_D < 0$ are plotted as a function of temperature in Figs. 4(c) and 4(d), respectively. The effect of the TaS_2 phase change on the device current manifests as a sharp increase in the drive current for both TaS_2 and Ni injection, as indicated by the black arrows. The change in drain current (I_D) can be attributed to the change in the series resistance offered by the TaS_2 portion of the device due to the C-T phase transition. The fractional enhancement of the drive current during phase change is stronger at higher V_g due to reduced MoS_2 channel resistance.

The MoS_2 extrinsic electron mobility (i.e., the effect of series resistance in mobility calculation has not been de-embedded) in the heterojunction device has been extracted by using the relation $\mu = [L/(CW_{ox}V_D)] \times (dI_D/dV_g)$ where L is the channel length, W is the channel width, and C_{ox} is the back-gate-oxide capacitance. The peak extrinsic mobility decreases with an increase in temperature, as

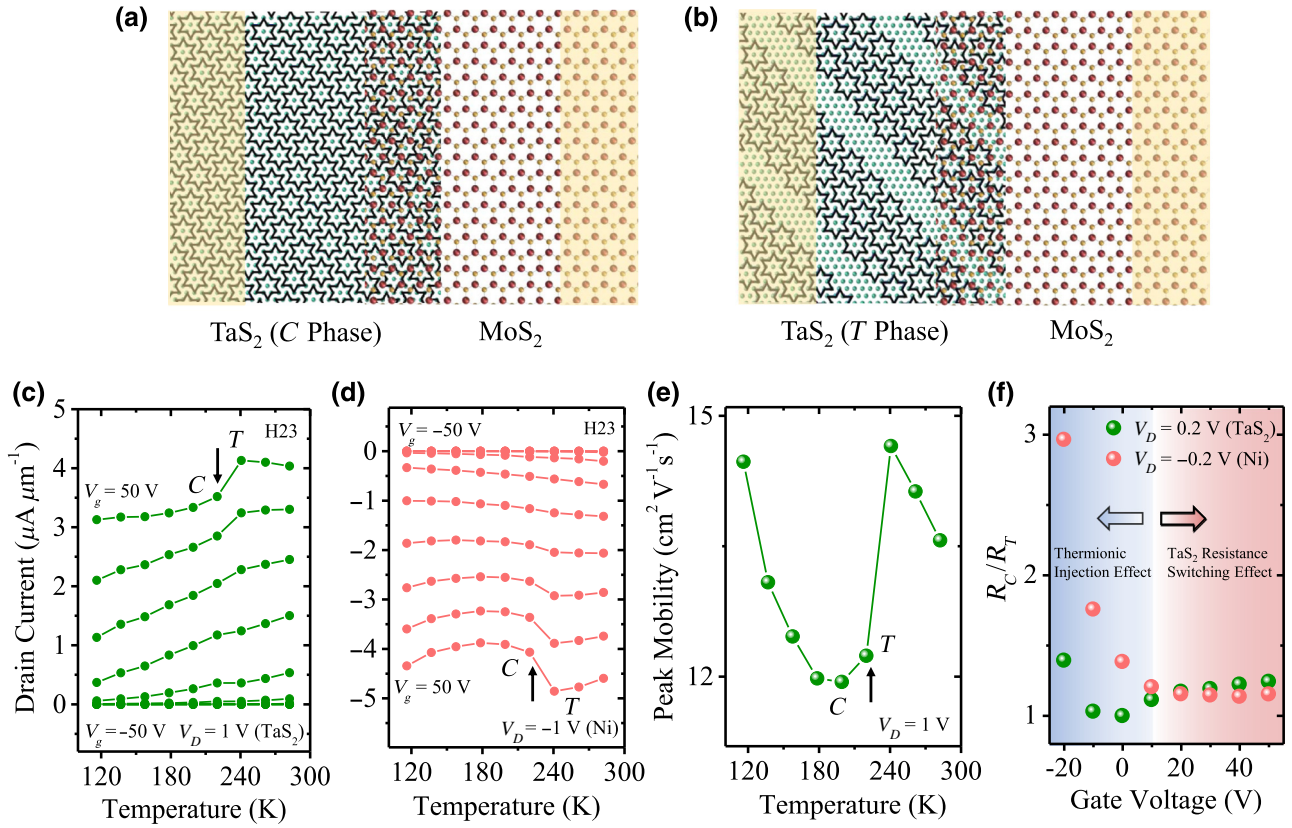

FIG. 4. Drive current impact of C-T phase transition in $1T$-$TaS_2/2H$-MoS_2 heterojunction device. (a),(b) Schematic of the heterojunction with TaS_2 in C phase [in (a)] and in T phase [in (b)]. (c),(d) Drive current of device H23 under $V_D > 0$ [in (c)] and $V_D < 0$ [in (d)]. The C-T phase transition temperature of TaS_2 is indicated by black arrows. (e) Temperature-dependent peak extrinsic mobility of H23. (f) Resistance ratio ($\rho = R_C/R_T$) dependence on the gate voltage for TaS_2 injection ($V_D = 0.2\,\mathrm{V}$) and Ni injection ($V_D = -0.2\,\mathrm{V}$).

shown in Fig. 4(e). Note that the suppression in the TaS_2 series resistance manifests itself by the sharp increase in the peak extrinsic mobility at the phase transition temperature, indicated by the black arrow.

Figure 4(f) shows the gate voltage dependence of the ratio of the measured resistances in the C phase and the T phase ($\rho = R_C/R_T$). Here, we define R_C and R_T as the total resistance measured right before (at 220 K) and right after (at 240 K) the C-T phase transition. At large negative V_g, the total resistance is governed by thermionic injection over the source-channel barrier and consequently, the ratio exponentially increases for the Ni injection case ($V_D = -0.2$ V) due to an increase in the temperature. However, at large positive V_g, where the current injection is dominated by tunneling through the Schottky barrier, the ratio becomes close to unity, but remains larger than 1. In fact, at larger positive V_g, the ratio increases with an increase in V_g. This effect is slightly more prominent in the TaS_2 injection ($V_D = 0.2$ V) case. Such an increase in the ratio is due to a gradual reduction in the MoS_2 channel resistance with V_g, and hence the effect due to TaS_2 series-resistance change becomes more pronounced.

D. Phase transition-induced SBH modulation and extraction of TaS_2 *C* phase Mott gap

In Fig. 4(f), we observe a surprisingly large difference in the ratio ρ in the TaS_2 and Ni injection cases when V_g is below the threshold voltage. ρ is found to be suppressed and strongly nonmonotonic in V_g at large negative V_g for the TaS_2 injection case, where the carrier injection is governed by thermionic injection over the Schottky barrier height. This suggests a change in the barrier height at the TaS_2/MoS_2 interface due to the C-T phase change. To explore the SBH at the TaS_2/MoS_2 heterojunction, in Fig. 5(a), we plot the H23 drain current (in log scale) at $V_D = 0.1$ V as a function of temperature for different gate voltages. As indicated by the dashed box, the device current is found to be suppressed by the C-T phase transition at low gate voltages, although this effect smears out at higher gate voltages. This suppression of current is contrary to the current enhancement effect at large V_g in Fig. 4(c). Note that at such a low gate voltage, the channel resistance is high, hence TaS_2 series resistance or channel mobility do not play any role in such flattening

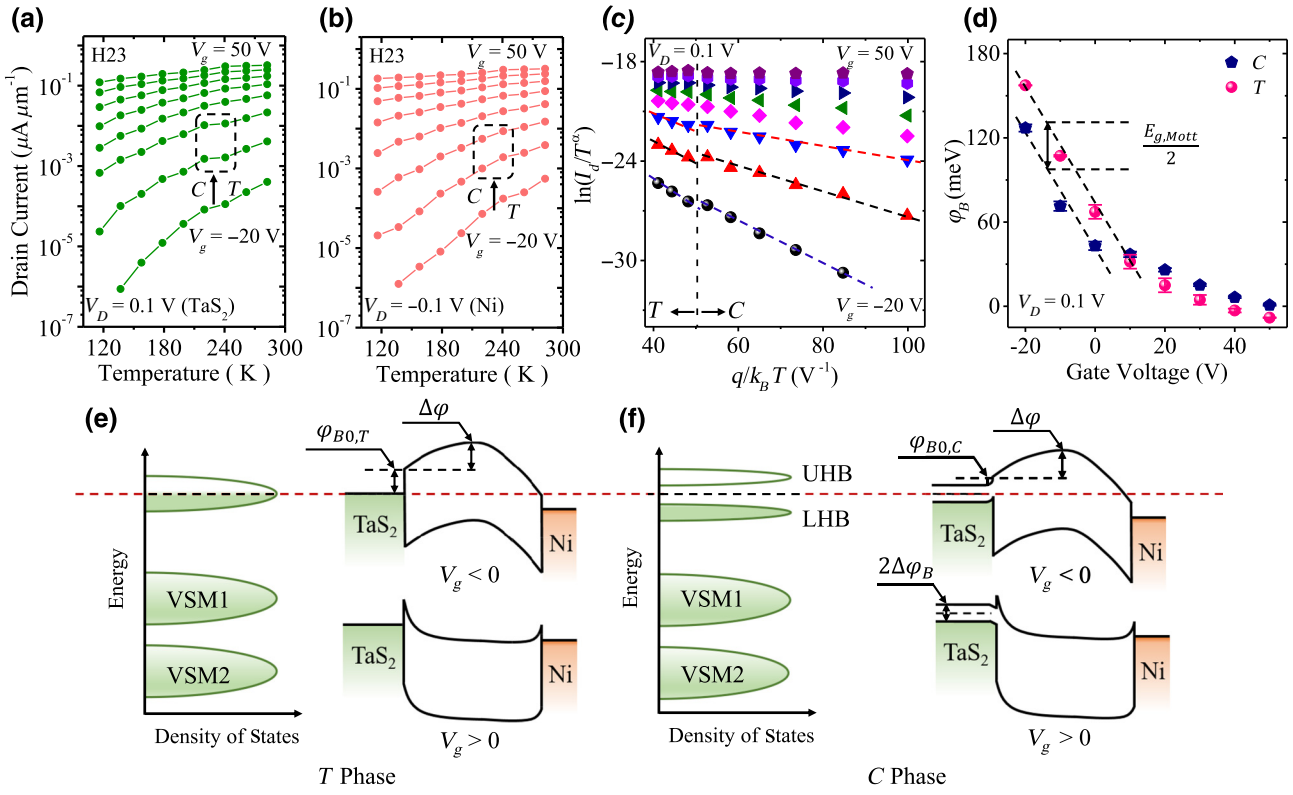

FIG. 5. Phase-dependent Schottky barrier height at 1T-TaS_2/2H-MoS_2 interface of H23 and Mott-gap estimation in C Phase of 1T-TaS_2. (a) Drain current as a function of temperature under small positive drain bias (TaS_2 injection). The dashed box indicates the suppression of drain current by the C-T phase transition under low V_g, which smears out at higher V_g. (b) Drain current as a function of temperature under small negative drain bias (Ni injection), showing no such suppression in the dashed box. (c) Richardson plot (with $\alpha = 1$) at different gate voltages in two different phases, indicating a C-T phase-transition-driven change in slope at negative V_g due to change in barrier height. (d) Extracted barrier height plotted as a function of gate voltage in two different phases. The dashed parallel lines indicate linear increase of barrier height for larger negative V_g. (e),(f) Schematic representation of the barrier height increase mechanism from C phase to T phase.

of the device current. This indicates an increase in the SBH at the TaS_2/MoS_2 contact interface once the phase change in TaS_2 sets in. At small V_g, the current injection is completely governed by thermionic emission over the TaS_2/MoS_2 barrier. An increase in the temperature increases the thermionic emission probability, but the *C*-*T* phase change abruptly increases the SBH, compensating for the temperature increase effect. Note that no such current suppression behavior is observed when Ni injects the electrons (i.e., for $V_D < 0$) into the MoS_2 channel [dashed rectangular box in Fig. 5(b)]. This is due to the lack of any phase change of the Ni source, unlike TaS_2, hence SBH at the Ni source remains the same before and after T_{CT}.

We extract the total effective barrier (φ_B) offered by the TaS_2/MoS_2 junction at a given V_g using the Richardson equation. As recently proposed [39], we use a modified Richardson equation for such a top contact geometry: $I_D = A^* T^\alpha e^{-q\varphi_B/k_B T}$ where A^* is the modified Richardson constant, q is the absolute value of electronic charge, k_B is the Boltzmann constant, and α is a constant with $1 \leq \alpha \leq 1.5$. This differs in the power of T from the Richardson equation typically used for the interface between a metal and a conventional bulk semiconductor owing to a change in the dimensionality. φ_B is extracted from the slope of $\log(I_D/T^\alpha)$ vs $q/k_B T$ as depicted in Fig. 5(c). One can clearly observe the abrupt increase in the slope as the phase transition happens, indicating an increase in φ_B in the T phase. The extracted φ_B is plotted in Fig. 5(d) as a function of V_g for both the C and T phases. We note here that the extracted φ_B is not very reliable at large positive V_g due to a strong tunneling current and mobility degradation with temperature, which tend to underestimate the extracted effective barrier height.

In Fig. 5(d), the extracted barrier height is found to increase linearly with a decrease in V_g when V_g is small. The "knee point" in the curve, where the barrier height deviates from linearity, is indicative of the true Schottky barrier height φ_{B0} (i.e., under a flat-band condition) of the TaS_2/MoS_2 interface [51]. This is much lower compared with the difference between the work function of $1T$-TaS_2 (5.2 eV) [52] and the electron affinity of multi-layer MoS_2 (4 eV) [53,54]. This suggests a strong Fermi-level pinning at the interface, close to the conduction band edge of MoS_2—supporting the excellent carrier injection efficiency through the interface. Such a strong Fermi-level pinning is a unique feature of a TaS_2/MoS_2 vdW contact, suggesting the vdW gap does not efficiently suppress the evanescent wave function of the TaS_2 states, likely resulting in metal-induced gap states (MIGS) [55] in MoS_2.

Note that the increase in barrier height with negative V_g in the C and T phases can be fitted by two parallel lines, as shown in Fig. 5(d). This observation indicates that the band bending ($\Delta\varphi$) in MoS_2 is similar in both cases at large negative V_g. This is schematically explained in Figs. 5(e) and 5(f), which allows us to write the total barrier as $\varphi_{B,p}(V_g) = \varphi_{B0,p} + \Delta\varphi(V_g)$, where $\varphi_{B0,p}$ is the true SBH of the TaS_2/MoS_2 interface (under a flat-band condition) and $p \in \{C, T\}$ represents the phase of TaS_2. Assuming a symmetric Mott-gap opening, $\Delta\varphi_B$ provides an estimate of the Mott gap in TaS_2 in the C phase:

$$\Delta\varphi_B = \varphi_{B,T} - \varphi_{B,C} \approx \varphi_{B0,T} - \varphi_{B0,C} \approx \frac{E_{g,\mathrm{Mott}}}{2}.$$

The vertical separation of the dashed fitting lines in Fig. 5(d) is an indicator of $\Delta\varphi_B$. The extracted Mott energy gap of TaS_2 in the C phase is estimated to be $E_{g,\mathrm{Mott}} \approx 71 \pm 7$ meV. This is in reasonable agreement with reported numbers in the literature from different optical techniques, viz., infrared reflectivity [20,21], time-resolved photoemission spectroscopy [9,22], angle-resolved photoemission spectroscopy [10,23,24], and angle-resolved inverse photoemission spectroscopy [25]—providing an independent verification using a pure electrical transport method.

E. Enhancing resistance switching during *NC-IC* phase transition

Figures 6(a) and 6(b) depict the temperature-dependent drain current characteristics from another device (H45) possessing a lower threshold voltage than H23, and the device is driven deep into the inversion by increasing the overdrive voltage. An optical image of the device H45, along with the control TaS_2 transport characteristics, are provided in S2 in the Supplemental Material [40]. In this device, we could modulate the drive current by as much as approximately 40% through the *C*-*T* phase change under a large-gate-overdrive condition. The strong suppression of the drive current at higher temperatures (beyond 223 K) is due to the temperature-induced mobility degradation effect. The temperature-dependent peak extrinsic mobility extracted from H45 is shown in S2 in the Supplemental Material [40]. When we drive the temperature of the device up to 360 K, which is beyond the *NC-IC* phase transition temperature at 353 K, we observe that the *NC-IC* phase transition manifests as a step jump in the drive current, both for TaS_2 and Ni injection cases as in Figs. 6(a) and 6(b), respectively. The corresponding resistance switching ratios $\{[R_{NC}(T = 350\ K)]/[R_{IC}(T = 360\ K)]\}$ at $V_D = \pm 0.2$ V are plotted in Fig. 6(c). For reference, we also show the ratio for the TaS_2 control as a dashed line in the same plot. For the TaS_2 injection case($V_D = 0.2$ V), the switching ratio is a strong function of V_g and is remarkably large at negative V_g reaching a value of 17.3 at $V_g = -80$ V, which is 14.5 times higher than the TaS_2 control device. On the other hand, the ratio remains a weak function of V_g for the Ni injection case and remains close to the value of the TaS_2 control.

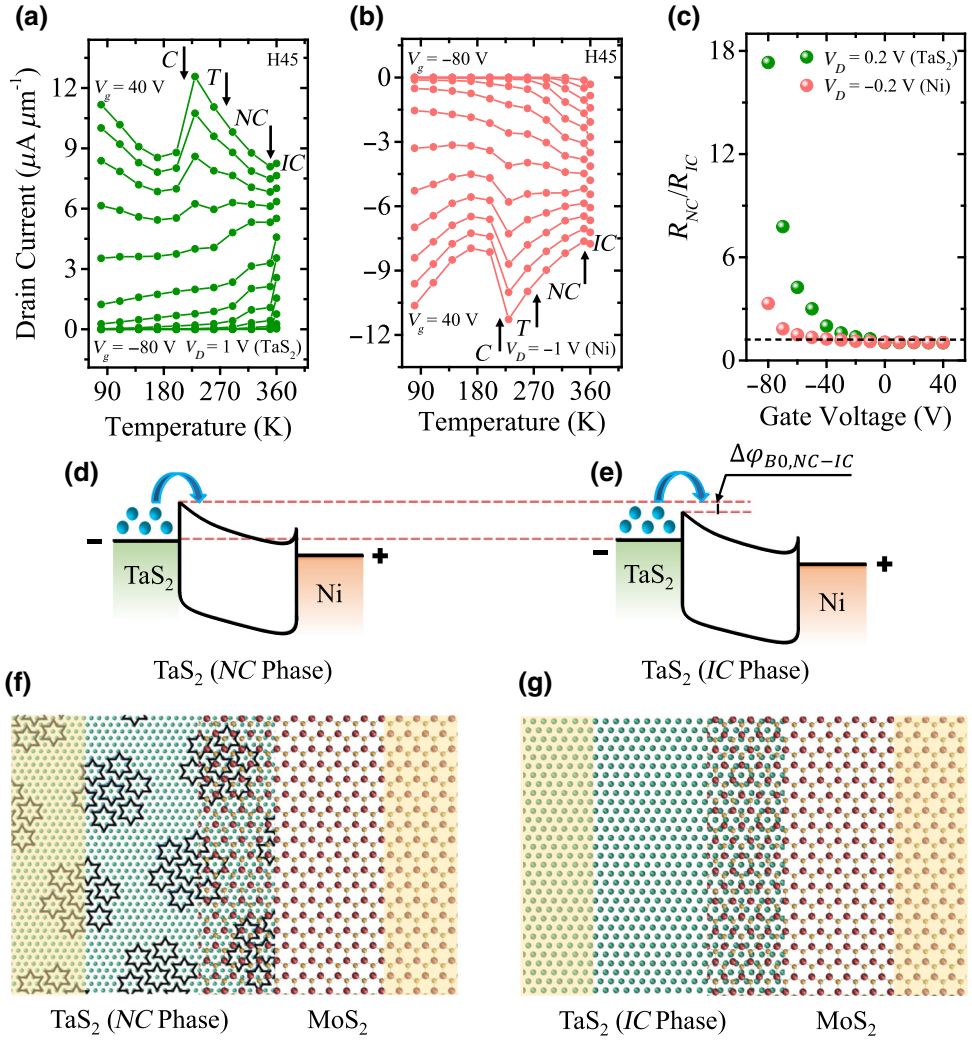

FIG. 6. Enhanced resistance switching during *NC*-*IC* phase transition in 1*T*-TaS_2/2*H*-MoS_2 heterojunction device H45. (a),(b) Drive current of device H45 under $V_D > 0$ [in (a)] and $V_D < 0$ [in (b)]. The different phase transition temperatures of TaS_2 are indicated by black arrows. (c) Resistance ratio (R_{NC}/R_{IC}) as a function of gate voltage for TaS_2 injection (in green symbols, $V_D = 0.2$ V) and Ni injection (in orange symbols, $V_D = -0.2$ V). The dashed line indicates 1*T*-TaS_2 control. (d),(e) Schematic for SBH height reduction from *NC* [in (d)] to *IC* phase [in (e)]. (f),(g) Schematic of the heterojunction with TaS_2 in *NC* phase [in (f)] and in *IC* phase [in (g)].

These observations point to a suppression of the SBH at the TaS_2/MoS_2 interface due to the *NC*-*IC* phase transition, as schematically depicted in Figs. 6(d)–6(g). Consequently, for electron injection from the TaS_2 source, the current modulation is much higher, while for Ni injection, we only get small effect due to a change in the series resistance of TaS_2 during the phase transition. While the origin of such a change in SBH requires further investigation, it is likely that during the *NC*-*IC* phase transition, as the hexagonal David-star clusters are broken [Figs. 6(f) and 6(g)] to increase conductivity, there is a more pronounced effect of the MIGS from TaS_2 into the band gap of MoS_2. This causes the Fermi level to be pinned closer to the conduction band edge of MoS_2, reducing the SBH.

III. CONCLUSION

In conclusion, we demonstrate a low-barrier-efficient electrical contact between a 1*T*-TaS_2 source and a 2*H*-MoS_2 channel, which is promising for "all-2D" flexible electronics. Along with the usual conductivity switching of 1*T*-TaS_2 during different phase transitions, we discover that these transitions also bring about a change in the Schottky barrier height at the 1*T*-TaS_2/2*H*-MoS_2 interface. The phase-transition-driven resistance-switching ratio of the heterojunction thus shows a large modulation that can be controlled by an external gate voltage. This enhancement and additional gate control provide an unprecedented opportunity for boosting different device applications that exploit such phase-transition-induced

resistance switching, such as broadband photodetection, neuromorphic circuits, negative differential conductance, and fast oscillators.

ACKNOWLEDGEMENTS

K.M. acknowledges a grant from the Indian Space Research Organization (ISRO), grants under Ramanujan Fellowship, Early Career Award, and Nano Mission from the Department of Science and Technology (DST), Government of India, and support from MHRD, MeitY, and the DST Nano Mission through NNetRA.

M. Mahajan and K. Murali contributed equally to this work.

[1] S. Z. Butler, S. M. Hollen, L. Cao, Y. Cui, J. A. Gupta, H. R. Gutiérrez, T. F. Heinz, S. S. Hong, J. Huang, A. F. Ismach, E. Johnston-Halperin, M. Kuno, V. V. Plashnitsa, R. D. Robinson, R. S. Ruoff, S. Salahuddin, J. Shan, L. Shi, M. G. Spencer, M. Terrones, W. Windl, and J. E. Goldberger, Progress, challenges, and opportunities in two-dimensional materials beyond graphene, ACS Nano **7**, 2898 (2013).

[2] D. Jariwala, V. K. Sangwan, L. J. Lauhon, T. J. Marks, and M. C. Hersam, Emerging device applications for semiconducting two-dimensional transition metal dichalcogenides, ACS Nano **8**, 1102 (2014).

[3] D. Akinwande, N. Petrone, and J. Hone, Two-dimensional flexible nanoelectronics, Nat. Commun. **5**, 1 (2014).

[4] R. E. Thorne, Charge-density-wave conductors, Phys. Today **49**, 42 (1996).

[5] G. Grüner, The dynamics of charge-density waves, Rev. Mod. Phys. **60**, 1129 (1988).

[6] J. A. Wilson, F. J. Di Salvo, and S. Mahajan, Charge-density waves and superlattices in the metallic layered transition metal dichalcogenides, Adv. Phys. **24**, 117 (1975).

[7] P. M. Williams, C. Scruby, W. Clark, and G. Parry, Charge density waves in the layered transition metal dichalcogenides, J. Phys. Colloq. **37**, C4 139 (1976).

[8] B. Sipos, A. F. Kusmartseva, A. Akrap, H. Berger, L. Forró, and E. Tutǐ, From Mott state to superconductivity in 1T-TaS_2, Nat. Mater. **7**, 960 (2008).

[9] S. Hellmann, M. Beye, C. Sohrt, T. Rohwer, F. Sorgenfrei, H. Redlin, M. Kalläne, M. Marczynski-Bühlow, F. Hennies, M. Bauer, A. Föhlisch, L. Kipp, W. Wurth, and K. Rossnagel, Ultrafast Melting of a Charge-Density Wave in the Mott Insulator 1T-TaS_2, Phys. Rev. Lett. **105**, 187401 (2010).

[10] K. Rossnagel, On the origin of charge-density waves in select layered transition-metal dichalcogenides, J. Phys. Condens. Matter. **23**, 213001 (2011).

[11] R. Manzke, T. Buslaps, B. Pfalzgraf, M. Skibowski, and O. Anderson, On the phase transitions in 1T-TaS_2, Europhys. Lett. **8**, 195 (1989).

[12] T. Ishiguro and H. Sato, Electron microscopy of phase transformations in 1T-TaS_2, Phys. Rev. B **44**, 2046 (1991).

[13] R. E. Thomson, B. Burk, A. Zettl, and J. Clarke, Scanning tunneling microscopy of the charge-density-wave structure in 1T-TaS_2, Phys. Rev. B **49**, 16899 (1994).

[14] T. Tani, T. Osada, and S. Tanaka, The pressure effect on the CDW-transition temperatures in 1T-TaS_2, Solid State Commun. **22**, 269 (1977).

[15] F. J. Di Salvo, J. A. Wilson, B. G. Bagley, and J. V. Waszczak, Effects of doping on charge-density waves in layer compounds, Phys. Rev. B **12**, 2220 (1975).

[16] R. Ang, Y. Tanaka, E. Ieki, K. Nakayama, T. Sato, L. J. Li, W. J. Lu, Y. P. Sun, and T. Takahashi, Real-Space Coexistence of the Melted Mott State and Superconductivity in Fe-Substituted 1T-TaS_2, Phys. Rev. Lett. **109**, 176403 (2012).

[17] M. Yoshida, Y. Zhang, J. Ye, R. Suzuki, Y. Imai, S. Kimura, A. Fujiwara, and Y. Iwasa, Controlling charge-density-wave states in nano-thick crystals of 1T-TaS_2, Sci. Rep. **4**, 07302 (2014).

[18] Y. Yu, F. Yang, X. F. Lu, Y. J. Yan, Y. H. Cho, L. Ma, X. Niu, S. Kim, Y. W. Son, D. Feng, S. Li, S. W. Cheong, X. H. Chen, and Y. Zhang, Gate-tunable phase transitions in thin flakes of 1T-TaS_2, Nat. Nanotechnol. **10**, 270 (2015).

[19] D. Stojchevska, L. Vaskivvskyi, I. Mertelj, T. Svetin, D. Brazovskii, and S. Mihailovic, Ultrafast switching to a stable hidden quantum state in an electronic crystal, Science **344**, 177 (2014).

[20] A. S. Barker, J. A. Ditzenberger, and F. J. DiSalvo, Infrared study of the electronic instabilities in tantalum disulfide and tantalum diselenide, Phys. Rev. B **12**, 2049 (1975).

[21] L. V. Gasparov, K. G. Brown, A. C. Wint, D. B. Tanner, H. Berger, G. Margaritondo, R. Gaál, and L. Forró, Phonon anomaly at the charge ordering transition in 1T-TaS_2, Phys. Rev. B - Condens. Matter Mater. Phys. **66**, 943011 (2002).

[22] L. Perfetti, P. A. Loukakos, M. Lisowski, U. Bovensiepen, M. Wolf, H. Berger, S. Biermann, and A. Georges, Femtosecond dynamics of electronic states in the Mott insulator 1T-TaS_2 by time resolved photoelectron spectroscopy, New J. Phys. **10**, 053019 (2008).

[23] R. A. Pollak, D. E. Eastman, F. J. Himpsel, P. Heimann, and B. Reihl, 1T-TaS_2 charge-density-wave metal-insulator transition and Fermi-surface modification observed by photoemission, Phys. Rev. B **24**, 7435 (1981).

[24] T. Pillo, J. Hayoz, D. Naumović, H. Berger, L. Perfetti, L. Gavioli, A. Taleb-Ibrahimi, L. Schlapbach, and P. Aebi, Fine structure in high-resolution photoemission spectra of quasi-two-dimensional 1T-TaS_2, Phys. Rev. B **64**, 245105 (2001).

[25] H. Sato, M. Arita, Y. Utsumi, Y. Mukaegawa, M. Sasaki, A. Ohnishi, M. Kitaura, H. Namatame, and M. Taniguchi, Conduction-band electronic structure of 1T-TaS_2 revealed by angle-resolved inverse-photoemission spectroscopy, Phys. Rev. B - Condens. Matter Mater. Phys. **89**, 155137 (2014).

[26] D. Wu, Y. Ma, Y. Niu, Q. Liu, T. Dong, S. Zhang, J. Niu, H. Zhou, J. Wei, Y. Wang, Z. Zhao, and N. Wang, Ultrabroadband photosensitivity from visible to terahertz at room temperature, Sci. Adv. **4**, eaao3057 (2018).

[27] G. Liu, B. Debnath, T. R. Pope, T. T. Salguero, R. K. Lake, and A. A. Balandin, A charge-density-wave oscillator based on an integrated tantalum disulfide-boron

nitride-graphene device operating at room temperature, Nat. Nanotechnol. **11**, 845 (2016).
[28] A. Khitun, G. Liu, and A. A. Balandin, Two-dimensional oscillatory neural network based on room temperature charge-density-wave devices, IEEE Trans. Nanotechnol. **16**, 860 (2017).
[29] P. A. Young, Lattice parameter measurements on molybdenum disulphide, J. Phys. D. Appl. Phys. **1**, 936 (1968).
[30] A. Spijkerman, J. L. de Boer, A. Meetsma, G. A. Wiegers, and S. van Smaalen, X-Ray crystal-structure refinement of the nearly commensurate phase of 1T-TaS_2 in $(3+2)$-dimensional superspace, Phys. Rev. B **56**, 13757 (1997).
[31] Y. T. Lee, K. Choi, H. S. Lee, S. W. Min, P. J. Jeon, D. K. Hwang, H. J. Choi, and S. Im, Graphene versus ohmic metal as source-drain electrode for MoS_2 nanosheet transistor channel, Small **10**, 2356 (2014).
[32] Y. Du, L. Yang, J. Zhang, H. Liu, K. Majumdar, P. D. Kirsch, and P. D. Ye, MoS_2 field-effect transistors with graphene/metal heterocontacts, IEEE Electron Device Lett. **35**, 599 (2014).
[33] W. S. Leong, X. Luo, Y. Li, K. H. Khoo, S. Y. Quek, and J. T. L. Thong, Low resistance metal contacts to MoS_2 devices with nickel-etched-graphene electrodes, ACS Nano **9**, 869 (2015).
[34] S. Andleeb, J. Eom, N. R. Naz, and A. K. Singh, MoS_2 field effect transistor with graphene contacts, J. Mater. Chem. C **5**, 8308 (2017).
[35] Y. Sata, R. Moriya, S. Masubuchi, K. Watanabe, T. Taniguchi, and T. Machida, N- and p-type carrier injections into WSe_2 with van Der Waals contacts of two-dimensional materials, Jpn. J. Appl. Phys. **56**, 04CK09 (2017).
[36] H. G. Shin, H. S. Yoon, J. S. Kim, M. Kim, J. Y. Lim, S. Yu, J. H. Park, Y. Yi, T. Kim, S. C. Jun, and S. Im, Vertical and in-plane current devices using NbS_2/n-MoS_2 van Der Waals Schottky junction and graphene contact, Nano Lett. **18**, 1937 (2018).
[37] L. Yang, K. Majumdar, H. Liu, Y. Du, H. Wu, M. Hatzistergos, P. Y. Hung, R. Tieckelmann, W. Tsai, C. Hobbs, and P. D. Ye, Chloride molecular doping technique on 2D materials: WS_2 and MoS_2, Nano Lett. **14**, 6275 (2014).
[38] C. D. English, G. Shine, V. E. Dorgan, K. C. Saraswat, and E. Pop, Improved contacts to MoS_2 transistors by ultra-high vacuum metal deposition, Nano Lett. **16**, 3824 (2016).
[39] D. Somvanshi, S. Kallatt, C. Venkatesh, S. Nair, G. Gupta, J. K. Anthony, D. Karmakar, and K. Majumdar, Nature of carrier injection in metal/2D-semiconductor interface and its implications for the limits of contact resistance, Phys. Rev. B **96**, 205423 (2017).
[40] See Supplemental Material at http://link.aps.org/supplemental/10.1103/PhysRevApplied.11.024031 for output characteristics of the MoS_2 channel with Ni contact on both sides, characteristics of the TaS_2 control and the heterojunction from device H45.
[41] J. E. Smith, J. C. Tsang, and M. W. Shafer, Raman spectra of several layer compounds with charge density waves, Solid State Commun. **19**, 283 (1976).
[42] J. R. Duffey, R. D. Kirby, and R. V. Coleman, Raman scattering from 1T-TaS_2, Solid State Commun. **20**, 617 (1976).
[43] S. Sugai, S. Murase, K. Uchida, and S. Tanaka, Comparison of the soft modes in tantalum dichalcogenides, Phys. B+C **105**, 405 (1981).
[44] W. Fu, Y. Chen, J. Lin, X. Wang, Q. Zeng, J. Zhou, L. Zheng, H. Wang, Y. He, H. He, Q. Fu, K. Suenaga, T. Yu, and Z. Liu, Controlled synthesis of atomically thin 1T-TaS_2 for tunable charge density wave phase transitions, Chem. Mater. **28**, 7613 (2016).
[45] R. He, J. Okamoto, Z. Ye, G. Ye, H. Anderson, X. Dai, X. Wu, J. Hu, Y. Liu, W. Lu, Y. Sun, A. N. Pasupathy, and A. W. Tsen, Distinct surface and 1bulk charge density waves in ultrathin 1T$-TaS_2$, Phys. Rev. B **94**, 201108 (2016).
[46] E. Tosatti and P. Fazekas, On the nature of the low-temperature phase of 1T-TaS_2, J. Phys. Colloq. **37**, C4-165 (1976).
[47] P. Fazekas and E. Tosatti, Structural and magnetic properties of pure and doped 1T-TaS_2, Philos. Mag. B **39**, 229 (1979).
[48] N. V. Smith, S. D. Kevan, and F. J. DiSalvo, Band structures of the layer compounds 1T-TaS_2 and 2H-$TaSe_2$ in the presence of commensurate charge-density waves, J. Phys. C Solid State Phys. **18**, 3175 (1985).
[49] K. Rossnagel and N. V. Smith, Spin-orbit coupling in the band structure of reconstructed 1T$-TaS_2$, Phys. Rev. B **73**, 073106 (2006).
[50] M. Núñez-Regueiro, J. Lopez-Castillo, and C. Ayache, Thermal conductivity of 1T-TaS_2 and 2H-$TaSe_2$, Phys. Rev. Lett. **55**, 1931 (1985).
[51] S. Das, H. Y. Chen, A. V. Penumatcha, and J. Appenzeller, High performance multilayer MoS_2 transistors with scandium contacts, Nano Lett. **13**, 100 (2013).
[52] T. Shimada and F. S. Ohuchi, Work function and photothreshold of layered metal dichalcogenides, Jpn. J. Appl. Phys. **33**, 2696 (1994).
[53] R. Schlaf, O. Lang, C. Pettenkofer, and W. Jaegermann, Band lineup of layered semiconductor heterointerfaces prepared by van Der Waals epitaxy: Charge transfer correction term for the electron affinity rule, J. Appl. Phys. **85**, 2732 (1999).
[54] S. L. Howell, D. Jariwala, C. C. Wu, K. S. Chen, V. K. Sangwan, J. Kang, T. J. Marks, M. C. Hersam, and L. J. Lauhon, Investigation of band-offsets at monolayer-multilayer MoS_2 junctions by scanning photocurrent microscopy, Nano Lett. **15**, 2278 (2015).
[55] J. Tersoff, Schottky Barrier Heights and the Continuum of Gap States, Phys. Rev. Lett. **52**, 465 (1984).